Bifurcation and hysteresis phenomena in two-dimensional sail-sail-flow interactions

Takeshi Sugimoto[a)]
Department of Information-Systems Creation, Kanagawa University, Yokohama, 221-8686, Japan

(Received 27 February 2007; accepted 16 October 2007; published online 7 December 2007)

This is the first report of complex bifurcation and manyfold hysteresis phenomena in the physics behind a pair of sails set in a flow of two dimensions. The formalism is based on inviscid vorticity theory, and the basic equations consist of a pair of integro-differential equations subject to a pair of nonlinear integral constraints. The method of solution is built up with the boundary element method for the integro-differential equations as well as the Newton–Raphson method for parameter search by use of the nonlinear integral constraints. Three types of configurations are considered as case studies on effects due to overlapping of the jib sail upon the main sail. Numerical analyses predict three sets of solutions: The convex-convex sail shapes, the concave-convex sail shapes, and the concave-concave sail shapes as well as two- or threefold hysteresis in aerodynamic and structural characteristics. Experimental observations confirm the existence of all the three solution sets, and moreover another set, the convex-concave sail shapes, is found by the experiment. The three case studies show that too much overlap of sails fails to obtain high lift. © *2007 American Institute of Physics*. [DOI: 10.1063/1.2818229]

I. INTRODUCTION

In most cases the flow field is determined by the geometry of the boundaries. But if the boundaries are compliant, flow-structure interactions take place and yield complex phenomena. Aerodynamics of sails is a typical example of the flow-structure interactions. We know that even the single sail problem is complex enough owing to many experimental, theoretical, and numerical works done so far. The present work provides a clue to multiple sail problems and shows the discovery of the bifurcation phenomena as a result of numerical prediction and experimental observations.

First, we shall very briefly review a study in a two-dimensional sail. Nonlinearity in sail-flow interactions yields hysteresis in aerodynamic and structural characteristics, because two equilibria exist within a certain range in the angle of attack: one has a bow-like camber and another has an S-shaped camber. An inviscid theory for an inextensible sail was first developed by Voelz[1] and then rediscovered by Thwaites[2] and Nielsen[3] independently. Several experiments were later carried out and compared with the inviscid theory.[4–6] The inviscid theory agrees fairly well with experiments insofar as experimental conditions fit to small-disturbance assumption. In the case of a single sail problem, bifurcation and hysteresis is well summarized by Murai and Maruyama.[7] Last efforts are concentrated on the development of viscous theories.[8,9]

There are practical needs for theories of three-dimensional sails to predict aerodynamic and structural characteristics of sails for yachts, hang gliders, and so on. Jackson and Christie[10] propose a general lifting surface theory for an elastic sail. In the special case of a circular elastic membrane in a flow[11] two equilibria are found in both the theory and the experiment. Lifting line theories are also available for elastic sails[12–14] and inextensible sails.[15,16]

There are very few papers that handle the interactions among a pair of flexible sails and a flow,[17,18] because it is difficult to find physically meaningful sets of tensions acting on a pair of structurally independent sails in a flow.

Myall and Berger[17] actually looked for the solution in which the suction force at the leading edge vanishes as the title of their paper shows. In their *eigenvalue* problem the tensions and sail shapes in equilibrium are found as the eigenvalues and the corresponding eigenvectors. That is why they treated this case only. It should be noted that these situations occur essentially at zero angle of attack in the case of the special configurations of sails.

Jackson[18] introduced an iteration to the formalism and solved the sail-sail-flow problem to show the usefulness of the iterative process. The result shows a single equilibrium at each angle of attack.

Thus far, the former studies describe restricted, not global, behavior of aerodynamic and structural interactions among a pair of sails and a flow. Hence there are few clues to the existence of multiple equilibria in the sail-sail-flow interactions. Our knowledge is quite limited with respect to interactions among a pair of flexible sails and a flow, even if it is two-dimensional and inviscid. Before going into a complex practical world, it is worthy for us to consider simpler but fundamental case studies.

We shall formulate the two-dimensional problem about the interactions among a pair of sails and a flow around them. As mentioned above, it is crucial to break the difficulty of determining forces acting on structurally independent sails. To do this, we explore the parameter space spanned by tensions acting on sails by a systematic search, i.e., the Newton–Raphson method. To obtain free mobility in this pa-

[a)]Electronic mail: take@is.kanagawa-u.ac.jp.

 © 2007 American Institute of Physics

Downloaded 09 Dec 2007 to 61.204.235.6. Redistribution subject to AIP license or copyright; see http://pof.aip.org/pof/copyright.jsp

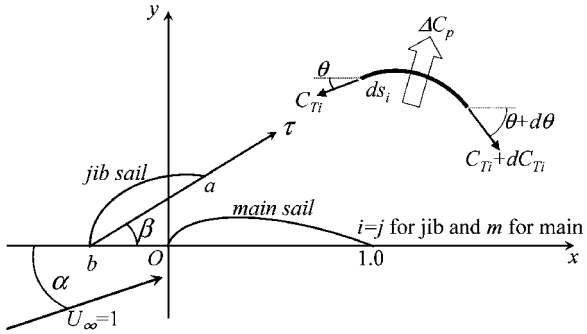

FIG. 1. The coordinate system and the notations. The formalism utilizes the Cartesian coordinate (x,y) with τ-axis along the jib sail with its origin at $(b,0)$ and tilted at the angle β to the x-axis; all the lengths are normalized by use of the chord length of the main sail, while the velocity is normalized by use of the uniform flow; the angle of attack α is defined as the main sail; the upper inset shows the tension C_{T_i} and the pressure difference ΔC_p acting on a sail element of length ds_i and slope angle θ.

rameter space and at the same time to ease the computational loads of the search, we sacrifice a part of reality by introducing the inviscid flow theory. This strategy is essentially indispensable to invent the numerical scheme, because we are led to the tractable formalism that consists of a pair of linear integro-differential equations associated with a pair of nonlinear constraints on sail lengths. To solve the integro-differential equations, we make use of the boundary element method. As a result of our numerical analysis we discover the complex bifurcation phenomena in the sail-sail-flow interactions, which we verify qualitatively by conducting experiments to observe the phenomena.

The present paper consists of five sections starting from this introduction; in Sec. II is the theory where the basic equations are derived and the method of solution is explained; in Sec. III is a detailed description of the experiments; in Sec. IV the numerical results as well as the observations in the experiments are discussed and annotated; Sec. V is the summary of our findings.

II. THEORY

A. Basic equations

To handle the sail-sail-flow interactions is on the line of practical needs to understand the behaviors of jib and main sails in action.

Figure 1 shows the coordinate system and the notations to be used in our study. The flow is approximated as incompressible and inviscid. This assumption is justified, partly because typical Reynolds numbers of phenomena are of the order of 10^7 for sailing craft, and partly because the aim of the spanning jib sails is to prevent flow separation over the main sail. Adding that, the former studies[4–6] show the good agreement between the inviscid thin-wing theory and the experiments for such small camber sails that we consider here.

The uniform flow with its velocity U approaches the sails at the angle α to the x axis. We denote α as the angle of attack. We nondimensionalize every quantity by use of c, the chord length of the main sail, and U.

Two sails are fixed and freely rotated at the leading and trailing edges; the leading edge of a sail is called the luff, while the trailing edge of a sail is called the leach. The luff and leech of the main sail are located upon the x axis, while the luff and leech of the jib sail are located upon the τ coordinate. The origin of the τ coordinate and β, the angle between the τ and x coordinates, are set to reflect the actual situation of the jib and main sails: (1) The luff of the jib sail is just on the center line of a sailing craft; (2) the leech of the jib sail root is fixed to the starboard side of the craft, i.e., the right side. The parameter a is the ratio of the jib chord-length to that of the main sail. The origin of the τ coordinate is located at the point $(x,y)=(-b,\ 0)$.

Sails are treated as inextensible, impervious, and infinitesimally thin materials. Deformation of the sails takes place due to slackness of the sails. We take s_j and s_m coordinates along the arcs of the jib and main sails, respectively. The angle of the slope to the x axis, designated by θ, is measured positive in a counterclockwise direction. Since the sails are set upright, we can neglect the effect due to gravity.

Since we are interested in upwind sails, α is a small angle. The angle β is small as well, because sailing craft are very narrow. We also insist that aerodynamic disturbances due to the sails are small. In due course we will neglect the higher order effects due to these small disturbances, i.e., γ, the bound vorticities on the sails. Now we shall derive the basic equations from the flow tangency condition and the mechanical equilibrium between the aerodynamic pressure and tensions.

A control point is defined as the point where the boundary condition is to be satisfied; a source point is the location of the vorticity; r and δ denote, respectively, the distance between the control and source points and the relative angle between them measured in the same sense of θ.

As Biot-Savart's law gives the velocity induced by the vorticity as $\gamma/2\pi r$, we have the boundary condition, i.e., the flow tangency condition; the slope of the boundary is equal to the ratio of the y-component of the velocity, v, to the x-component, u. Hence we have

$$\tan\theta=\frac{\mathrm{d}y}{\mathrm{d}x}=\frac{v}{u}$$
$$=\frac{\sin\alpha+\frac{1}{2\pi}\int_0^a\gamma\frac{\cos\delta}{r}\mathrm{d}\eta+\frac{1}{2\pi}\int_0^1\gamma\frac{\cos\delta}{r}\mathrm{d}\xi}{\cos\alpha-\frac{1}{2\pi}\int_0^a\gamma\frac{\sin\delta}{r}\mathrm{d}\eta-\frac{1}{2\pi}\int_0^1\gamma\frac{\sin\delta}{r}\mathrm{d}\xi}$$
$$\approx\alpha+\frac{1}{2\pi}\int_0^a\gamma\frac{\cos\delta}{r}\mathrm{d}\eta+\frac{1}{2\pi}\int_0^1\gamma\frac{\cos\delta}{r}\mathrm{d}\xi. \qquad (1)$$

In the last approximation we neglected the higher-than-third-order terms of small disturbances.

Moreover we approximate measurements of δ and r between a source point and a field point by using the points projected from the arc s_j or s_m upon the τ or x coordinate, respectively. Therefore the first integral on the right-hand side of Eq. (1) shall be taken along the τ coordinate, while the second integral shall be along the x axis. This is the

Downloaded 09 Dec 2007 to 61.204.235.6. Redistribution subject to AIP license or copyright; see http://pof.aip.org/pof/copyright.jsp

thin-wing approximation, which disregards the second-order error in $\cos\delta/r$ in Eq. (1); that term is multiplied by γ; therefore the error becomes the third order, and hence we consistently retain the second order accuracy in Eq. (1) by the thin-wing approximation.

The inset of Fig. 1 shows the mechanical boundary condition, i.e., the equilibrium between the tension and aerodynamic pressure acting on a sail element. The nondimensional tension coefficient is designated by C_{Ti} where the subscript i denotes either j or m for the jib or main sail, respectively. The pressure difference coefficient is designated by ΔC_P.

In the normal plane to the sail element the equilibrium is expressed by

$$\Delta C_P = -C_{Ti}\frac{\mathrm{d}\theta}{\mathrm{d}s_i}, \tag{2}$$

and in the tangent plane of the sail element by

$$\frac{\mathrm{d}C_{Ti}}{\mathrm{d}s_i} = 0. \tag{3}$$

Equation (3) shows that each tension is constant along the corresponding arc.

On the other hand the linearized Bernoulli's theorem leads us to the relation between the pressure difference and the bound vorticity on surfaces of the sails (see Ref. 19, p. 114, for example),

$$\Delta C_P \approx 2\gamma, \tag{4}$$

and hence Eq. (2) becomes

$$2\gamma = -C_{Ti}\frac{\mathrm{d}\theta}{\mathrm{d}s_i}. \tag{5}$$

Here we should note that ΔC_P for the infinitesimally thin wings does not contain the second-order perturbation (see Ref. 20, pp. 151-156, for example). Now we shall introduce deviation angles, ϵ_j for the jib sail and ϵ_m for the main sail, such that

$$\theta = \begin{cases} \beta + \epsilon_j & \text{for the jib sail,} \\ \epsilon_m & \text{for the main sail.} \end{cases} \tag{6}$$

First of all we shall recall

$$\alpha \ll 1 \quad \text{and} \quad \beta \ll 1.$$

Since slackness of each sail is small enough,

$$\epsilon_j \ll 1 \quad \text{and} \quad \epsilon_m \ll 1.$$

Therefore we have

$$\tan\theta \approx \begin{cases} \beta + \epsilon_j & \text{for the jib sail,} \\ \epsilon_m & \text{for the main sail,} \end{cases} \tag{7}$$

and

$$\frac{\mathrm{d}\theta}{\mathrm{d}s_i} = \begin{cases} \dfrac{\mathrm{d}\epsilon_j}{\mathrm{d}s_j} & \text{for the jib sail,} \\ \dfrac{\mathrm{d}\epsilon_m}{\mathrm{d}s_m} & \text{for the main sail.} \end{cases} \tag{8}$$

After eliminating γ from Eq. (1) by use of Eq. (5), and then substituting Eqs. (7) and (8) for Eq. (1), we arrive at

$$\epsilon_j + \frac{C_{T_j}}{4\pi}\int_0^a \frac{\mathrm{d}\epsilon_j}{\mathrm{d}s_j}\frac{\cos\delta}{r}\mathrm{d}\eta + \frac{C_{T_m}}{4\pi}\int_0^1 \frac{\mathrm{d}\epsilon_m}{\mathrm{d}s_m}\frac{\cos\delta}{r}\mathrm{d}\xi = \alpha - \beta \tag{9}$$

for the jib sail, and

$$\epsilon_m + \frac{C_{T_j}}{4\pi}\int_0^a \frac{\mathrm{d}\epsilon_j}{\mathrm{d}s_j}\frac{\cos\delta}{r}\mathrm{d}\eta + \frac{C_{T_m}}{4\pi}\int_0^1 \frac{\mathrm{d}\epsilon_m}{\mathrm{d}s_m}\frac{\cos\delta}{r}\mathrm{d}\xi = \alpha \tag{10}$$

for the main sail. Further noting

$$\frac{\mathrm{d}\epsilon_j}{\mathrm{d}s_j} \approx \frac{\mathrm{d}\epsilon_j}{\mathrm{d}\eta} \quad \text{and} \quad \frac{\mathrm{d}\epsilon_m}{\mathrm{d}s_m} \approx \frac{\mathrm{d}\epsilon_m}{\mathrm{d}\xi},$$

we are lead to a pair of the integro-differential equations in terms of unknowns ϵ_j and ϵ_m,

$$\epsilon_j(\tau) + \lambda_j\int_0^a \frac{\mathrm{d}\epsilon_j}{\mathrm{d}\eta}k(\tau,\eta)\mathrm{d}\eta + \lambda_m\int_0^1 \frac{\mathrm{d}\epsilon_m}{\mathrm{d}\xi}k(\tau,\xi)\mathrm{d}\xi = \alpha - \beta \tag{11}$$

and

$$\epsilon_m(x) + \lambda_j\int_0^a \frac{\mathrm{d}\epsilon_j}{\mathrm{d}\eta}k(x,\eta)\mathrm{d}\eta + \lambda_m\int_0^1 \frac{\mathrm{d}\epsilon_m}{\mathrm{d}\xi}k(x,\xi)\mathrm{d}\xi = \alpha, \tag{12}$$

where

$$\lambda_i = \frac{C_{Ti}}{4\pi}$$

and

$$k(p_c,p_s) = \frac{\cos\delta}{r}.$$

In the kernel function the indices p_c and p_s denote the locations of the control and source points, respectively.

Equations (11) and (12) become homogeneous if and only if both α and β become zero. But β is never zero, and hence we do not need to consider the eigenvalue problem.

There are nonlinear constraints on slackness of each sail. Suppose the total arc lengths of the sails are l_j and l_m, then we define slackness parameters as follows:

$$SR_j = \frac{l_j - a}{a} \quad \text{for the jib sail,} \tag{13}$$

and

$$SR_m = l_m - 1 \quad \text{for the main sail.} \tag{14}$$

We reduce the constraints on slackness as follows:

Downloaded 09 Dec 2007 to 61.204.235.6. Redistribution subject to AIP license or copyright; see http://pof.aip.org/pof/copyright.jsp

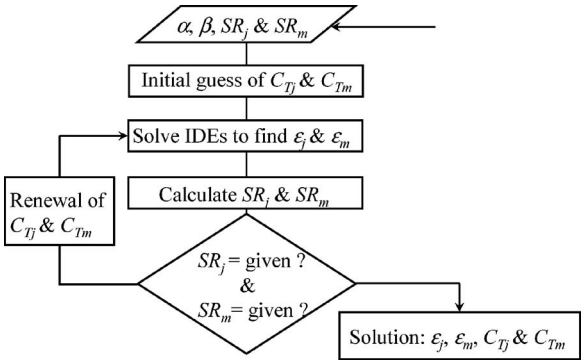

FIG. 2. The schema of the solution method. The method consists of the boundary element method to find the shapes of sails and the Newton–Raphson method to determine the tensions.

$$SR_j = \frac{\int_0^{l_j} \mathrm{d}s_j - a}{a} = \frac{\int_0^a \mathrm{d}\tau/\cos\epsilon_j - a}{a} \approx \frac{1}{2a}\int_0^a \epsilon_j^2 \mathrm{d}\tau \tag{15}$$

for the jib sail and in the very same manner

$$SR_m \approx \frac{1}{2}\int_0^1 \epsilon_m^2 \mathrm{d}x \tag{16}$$

for the main sail.

Now we have two unknown functions, ϵ_j and ϵ_m, and two unknown parameters, C_{T_j} and C_{T_m}, for a pair of integro-differential equations (11) and (12), subject to a pair of functional constraints, (15) and (16). Therefore our problem is appropriately formulated. Thus we formulate the problem by consistently retaining the second-order accuracy.

Equations (11) and (12) can be rewritten as a pair of Fredholm equations of the second kind. This implies that the existence of the solution is assured by the relevant general argument (see Ref. 21, pp. 49-80, for example).

B. Method of solution

Figure 2 shows the schema of the solution method. Given the parameters α, β, SR_j, and SR_m, we first solve the integro-differential equations (11) and (12) subject to the initial guess of C_{T_j} and C_{T_m}. Then we calculate the slackness parameters and renew the tensions if necessary. We shall repeat this iteration until we obtain the convergent solution set. To solve the integro-differential equations we use the boundary element method, in particular the vortex lattice method. To renew the tensions we make use of the Newton–Raphson method.

All I want to obtain is a tool to know if multiple equilibria exist subject to given geometry. In this respect I shall comment on the most important point in this numerical scheme. There is no iteration in finding the shapes, ϵ_j and ϵ_m, subject to given α, β, C_{T_j} and C_{T_m}. Just one calculation leads us to the solution. This becomes possible, because we introduce the thin-wing approximation. Our formalism, however, retains the second-order nonlinearity, in particular as slackness.

To search for the solution in the vast parameter space of $(\alpha, C_{T_j}, C_{T_m})$, we make the most of our knowledge on the single-sail and flow interactions[1–7] at the large angles of attack there exists the unique solution set, while near the zero angle of attack there exits multiple solution sets. We start our calculation at $\alpha=20°$ with an arbitrary initial guess of C_{T_j}, C_{T_m}, and the sail shapes; the calculation quickly converges to the solution that becomes the basis of the initial guess at α slightly smaller than 20°; by making the angle of attack gradually smaller, we obtain one solution set consisting of the convex jib and convex main configuration mentioned in Sec. IV. Then we restart our calculation at $\alpha=-20°$, and the above-mentioned procedure leads us to another solution set consisting of the concave jib and convex main configuration or the concave jib and concave main configuration mentioned in Sec. IV. Finally at $\alpha=0$ we try some more search by use of the initial guess that consists of the concave jib and convex main configuration or the convex jib and concave main configuration. In some cases this search leads us to the third solution set. The search process is pretty sensitive to the initial sail shapes and less sensitive to the initial guess of C_{T_j} and C_{T_m}.

We divide the jib and main sails into N_j and N_m panels, respectively. In our numerical analysis $N_j=N_m=40$. To obtain the curvature, however, it is necessary to use N_j+1 and N_m+1 slope data of the jib and main sails, respectively. We adopt the slope data at nodes, i.e., $\{\epsilon_{j_k}\}_{k=0,1,\ldots,N_j}$ for the jib sail and $\{\epsilon_{m_n}\}_{n=0,1,\ldots,N_m}$ for the main sail. The vortex lattice method adopts constant length panels, a quarter point of each panel for a source point, and three quarters point of each panel for a control point. This configuration of control and source points is known to lead us to the very accurate results (see for example, Ref. 19, pp. 264–265). Therefore we have the slope of the kth panel at three quarters point as follows:

$$\tilde{\epsilon}_{i_k} = \frac{3\epsilon_{i_k} + \epsilon_{i_{k-1}}}{4}, \tag{17}$$

where $\tilde{\epsilon}_{i_k}$ and ϵ_{i_k} denote the slope at the control point and that at the edge of the kth panel, respectively.

At the source points we need the curvature instead of the vorticity because of Eq. (5). This can be done in the same manner above,

$$\frac{\mathrm{d}\tilde{\epsilon}_{j_k}}{\mathrm{d}\eta} \approx \frac{\epsilon_{j_k} - \epsilon_{j_{k-1}}}{h_j}, \qquad \frac{\mathrm{d}\tilde{\epsilon}_{m_k}}{\mathrm{d}\xi} \approx \frac{\epsilon_{m_k} - \epsilon_{m_{k-1}}}{h_m}, \tag{18}$$

where h_j and h_m denote the panel lengths of the jib and main sails, respectively.

By discretizing Eqs. (11) and (12), we have

$$\tilde{\epsilon}_j(\tau_i) + \lambda_j \sum_{k=1}^{N_j} \frac{\mathrm{d}\tilde{\epsilon}_j}{\mathrm{d}\eta} k(\tau_i, \eta_k) h_j + \lambda_m \sum_{l=1}^{N_m} \frac{\mathrm{d}\tilde{\epsilon}_m}{\mathrm{d}\xi} k(\tau_i, \xi_l) h_m = \alpha - \beta \tag{19}$$

for $i=1,2,\ldots,N_j$ and

Downloaded 09 Dec 2007 to 61.204.235.6. Redistribution subject to AIP license or copyright; see http://pof.aip.org/pof/copyright.jsp

$$\tilde{\epsilon}_m(x_n) + \lambda_j \sum_{k=1}^{N_j} \frac{\mathrm{d}\tilde{\epsilon}_j}{\mathrm{d}\eta} k(x_n, \eta_k) h_j + \lambda_m \sum_{l=1}^{N_m} \frac{\mathrm{d}\tilde{\epsilon}_m}{\mathrm{d}\xi} k(x_n, \xi_l) h_m = \alpha \tag{20}$$

for $n=1,2,\ldots,N_m$.

Substituting Eqs. (17) and (18) for Eqs. (19) and (20), we obtain the final form of the equations to be solved,

$$\frac{3}{4}\epsilon_{j_i} + \frac{1}{4}\epsilon_{j_{i-1}} + \lambda_j \sum_{k=1}^{N_j} (\epsilon_{j_k} - \epsilon_{j_{k-1}}) k(\tau_i, \eta_k) + \lambda_m \sum_{l=1}^{N_m} (\epsilon_{m_l} - \epsilon_{m_{l-1}}) k(\tau_i, \xi_l) = \alpha - \beta \tag{21}$$

for $i=1,2,\ldots,N_j$ and

$$\frac{3}{4}\epsilon_{m_n} + \frac{1}{4}\epsilon_{m_{n-1}} + \lambda_j \sum_{k=1}^{N_j} (\epsilon_{j_k} - \epsilon_{j_{k-1}}) k(x_n, \eta_k) + \lambda_m \sum_{l=1}^{N_m} (\epsilon_{m_l} - \epsilon_{m_{l-1}}) k(x_n, \xi_l) = \alpha \tag{22}$$

for $n=1,2,\ldots,N_m$.

In this way we get N_j+N_m linear simultaneous equations, but the number of the unknowns is N_j+N_m+2.

To get two more equations we shall introduce the identities on the conditions that the sails are fixed at the leading and trailing edges,

$$\int_0^a \tan \epsilon_j \mathrm{d}\tau = 0,$$

and

$$\int_0^1 \tan \epsilon_m \mathrm{d}x = 0.$$

The left-hand sides of the identities above are approximately equal to

$$\int_0^a \epsilon_j \mathrm{d}\tau$$

and

$$\int_0^1 \epsilon_m \mathrm{d}x,$$

respectively. Carrying out integration by use of the trapezoidal rule with given panels, we obtain the two additional equations for unknowns,

$$\epsilon_{j_0} + 2\sum_{k=1}^{N_j-1} \epsilon_{j_k} + \epsilon_{j_{N_j}} = 0 \tag{23}$$

and

$$\epsilon_{m_0} + 2\sum_{n=1}^{N_m-1} \epsilon_{m_n} + \epsilon_{m_{N_m}} = 0. \tag{24}$$

A set of Eqs. (21)–(24) are linear in terms of the unknowns $\{\epsilon_{j_k}\}_{k=0,1,\ldots,N_j}$ and $\{\epsilon_{m_n}\}_{n=0,1,\ldots,N_m}$, and hence it is easy to solve subject to given C_{Tj} and C_{Tm}.

Thus the rest of the problem solving is how to renew the tensions toward the convergent solution. For this purpose we shall determine the tensions to fulfill the functional constraints on slackness of the sails, i.e., Eqs. (15) and (16). First we discretize these functionals. Suppose ϵ_i changes linearly over the kth panel from $\epsilon_{i_{k-1}}$ to ϵ_{i_k},

$$\epsilon_i(s_i) = \epsilon_{i_{k-1}}\left(1 - \frac{s_i}{h_i}\right) + \epsilon_{i_k}\frac{s_i}{h_i},$$

then integration of ϵ_i^2 over this panel yields the results,

$$\frac{h_i}{3}(\epsilon_{i_{k-1}}^2 + \epsilon_{i_{k-1}}\epsilon_{i_k} + \epsilon_{i_k}^2).$$

Therefore we obtain the quadrature necessary for calculating the slackness parameters,

$$\int_0^a \epsilon_j^2 \mathrm{d}\tau \approx \frac{h_j}{3}\sum_{k=1}^{N_l} (\epsilon_{j_{k-1}}^2 + \epsilon_{j_{k-1}}\epsilon_{j_k} + \epsilon_{j_k}^2) \tag{25}$$

and

$$\int_0^1 \epsilon_m^2 \mathrm{d}x \approx \frac{h_m}{3}\sum_{n=1}^{N_m} (\epsilon_{m_{n-1}}^2 + \epsilon_{m_{n-1}}\epsilon_{m_n} + \epsilon_{m_n}^2). \tag{26}$$

Using Eqs. (15), (16), (25), and (26), we shall define the implicit functions in terms of C_{Tj} and C_{Tm} by

$$F_j(C_{Tj}, C_{Tm}) \overset{\text{def}}{=} \frac{h_j}{6a}\sum_{k=1}^{N_l} (\epsilon_{j_{k-1}}^2 + \epsilon_{j_{k-1}}\epsilon_{j_k} + \epsilon_{j_k}^2) - SR_j \tag{27}$$

and

$$F_m(C_{Tj}, C_{Tm}) \overset{\text{def}}{=} \frac{h_m}{6}\sum_{n=1}^{N_m} (\epsilon_{m_{n-1}}^2 + \epsilon_{m_{n-1}}\epsilon_{m_n} + \epsilon_{m_n}^2) - SR_m. \tag{28}$$

Then we shall look for C_{Tj}^* and C_{Tm}^* that satisfy the constraints on the slackness,

$$\begin{bmatrix} F_j(C_{Tj}^*, C_{Tm}^*) \\ F_m(C_{Tj}^*, C_{Tm}^*) \end{bmatrix} = \begin{pmatrix} 0 \\ 0 \end{pmatrix}. \tag{29}$$

We find the solution set by use of the Newton–Raphson method, i.e.,

Downloaded 09 Dec 2007 to 61.204.235.6. Redistribution subject to AIP license or copyright; see http://pof.aip.org/pof/copyright.jsp

$$\begin{pmatrix} C_{Tj}^* \\ C_{Tm}^* \end{pmatrix} = \begin{pmatrix} C_{Tj} \\ C_{Tm} \end{pmatrix} - \begin{pmatrix} \dfrac{\partial F_j}{\partial C_{Tj}} & \dfrac{\partial F_j}{\partial C_{Tm}} \\ \dfrac{\partial F_m}{\partial C_{Tj}} & \dfrac{\partial F_m}{\partial C_{Tm}} \end{pmatrix}^{-1} \begin{bmatrix} F_j(C_{Tj}, C_{Tm}) \\ F_m(C_{Tj}, C_{Tm}) \end{bmatrix}, \quad (30)$$

where the left-hand sides are the new estimate of the tensions. To calculate the right-hand sides of Eq. (30), we need the derivatives of the functionals, which we shall approximate by use of the following finite differences:

$$\frac{\partial F_j}{\partial C_{Tj}} \approx \frac{F_j(C_{Tj}+\Delta, C_{Tm}) - F_j(C_{Tj}-\Delta, C_{Tm})}{2\Delta},$$

$$\frac{\partial F_j}{\partial C_{Tm}} \approx \frac{F_j(C_{Tj}, C_{Tm}+\Delta) - F_j(C_{Tj}, C_{Tm}-\Delta)}{2\Delta},$$

$$\frac{\partial F_m}{\partial C_{Tj}} \approx \frac{F_m(C_{Tj}+\Delta, C_{Tm}) - F_m(C_{Tj}-\Delta, C_{Tm})}{2\Delta},$$

$$\frac{\partial F_m}{\partial C_{Tm}} \approx \frac{F_m(C_{Tj}, C_{Tm}+\Delta) - F_m(C_{Tj}, C_{Tm}-\Delta)}{2\Delta},$$

where we take $\Delta = 10^{-9}$ for our numerical analysis. In every iteration we need to calculate five sets of $\{F_j, F_m\}$, but this process leads us very quickly to the convergent solution without much computing time.

To check the convergence, we impose the seven significant-digit accuracy upon the relative errors between the new and old values of the tensions.

Once we get the convergent solution set, i.e., $\{\epsilon_{j_k}\}_{k=0,1,\ldots,N_j}$, $\{\epsilon_{m_n}\}_{n=0,1,\ldots,N_m}$, C_{Tj} and C_{Tm}, then we estimate the aerodynamic characteristics in the following. The role of the jib sail is the same as a flap. To see how much lift is enhanced by use of the jib sail, we define the lift coefficient based on the chord length of the main sail alone,

$$\begin{aligned} C_l &= 2\int_0^{l_j} \gamma \mathrm{d}s_j + 2\int_0^{l_m} \gamma \mathrm{d}s_m \\ &= -C_{Tj}\int_0^{l_j} \frac{\mathrm{d}\epsilon_j}{\mathrm{d}s_j}\mathrm{d}s_j - C_{Tm}\int_0^{l_m} \frac{\mathrm{d}\epsilon_m}{\mathrm{d}s_m}\mathrm{d}s_m \\ &= -C_{Tj}[\epsilon_j(l_j) - \epsilon_j(0)] - C_{Tm}[\epsilon_m(l_m) - \epsilon_m(0)] \\ &= C_{Tj}(\epsilon_{j_0} - \epsilon_{j_{N_j}}) + C_{Tm}(\epsilon_{m_0} - \epsilon_{m_{N_m}}). \end{aligned} \quad (31)$$

The nose-up moment coefficient around the mast is defined by

$$\begin{aligned} C_m &= 2\int_0^a \gamma(b\cos\beta - \tau)\mathrm{d}\tau - 2\int_0^1 \gamma x \mathrm{d}x \\ &= -C_{Tj}\int_0^a \frac{\mathrm{d}\epsilon_l}{\mathrm{d}s_j}(b\cos\beta - \tau)\mathrm{d}\tau + C_{Tm}\int_0^1 \frac{\mathrm{d}\epsilon_m}{\mathrm{d}s_m} x\mathrm{d}x \\ &\approx -C_{Tj}\int_0^a \frac{\mathrm{d}\epsilon_l}{\mathrm{d}\tau}(b-\tau)\mathrm{d}\tau + C_{Tm}\int_0^1 \frac{\mathrm{d}\epsilon_m}{\mathrm{d}x} x\mathrm{d}x \\ &\approx -C_{Tj}\sum_{k=1}^{N_j} \frac{\epsilon_{j_k} - \epsilon_{j_{k-1}}}{h_j}\left\{b - h_j\left(k - \frac{1}{2}\right)\right\}h_j + C_{Tm}\sum_{n=1}^{N_m} \frac{\epsilon_{m_n} - \epsilon_{m_{n-1}}}{h_m}\left\{h_m\left(n - \frac{1}{2}\right)\right\}h_m \\ &= -C_{Tj}\sum_{k=1}^{N_j} (\epsilon_{j_k} - \epsilon_{j_{k-1}})\left\{b - h_j\left(k - \frac{1}{2}\right)\right\} + C_{Tm}\sum_{n=1}^{N_m} (\epsilon_{m_n} - \epsilon_{m_{n-1}})h_m\left(n - \frac{1}{2}\right). \end{aligned}$$

III. EXPERIMENTAL SETUP

We conduct experiments to observe small models in a small test bed and to confirm that the theoretical prediction is not spurious.

The apparatus we own is Air Flow Bench AF10 manufactured by TecQuipment. Figure 3(a) shows its appearance. This test bed provides air flow with the speed up to 30 m/s into the tiny test section: the section is 5.0 cm wide, 10 cm high, and 40 cm long in a streamwise direction; the observation window has circular panes with 9.5 cm diameter. The airway in the test bed is not fully closed, but wind circulates in the system. The test section is connected to the open end of the convergent air way down the settling chamber on top of the system.

We measure the in-process velocity by the Pitot static tube connected to the piezoelectric anemometer.

We prepare the three types of setup that correspond to the case studies provided by the numerical analysis; the

Downloaded 09 Dec 2007 to 61.204.235.6. Redistribution subject to AIP license or copyright; see http://pof.aip.org/pof/copyright.jsp

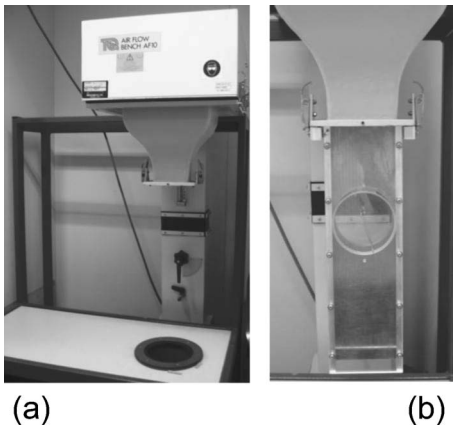

FIG. 3. Experimental apparatus and sail models in the test section. (a) The upright test bed: Wind blows from top to bottom; a centrifugal fan is located under the table; the duct behind the table is for supply air to the settling chamber on top of the system. (b) The test section: Circular parts house the model sails made of sheets of transparencies supported by steel rods at the both edges; circular panes are clamped to the test section and rotated to change the angle of attack.

chord lengths of sail used are 3.0 cm, 4.5 cm, and 6.0 cm, while the spans of all the models are the same 5.0 cm; as a sail material we make use of transparencies for presentation; at the edges the sail sheets are fixed to steel rods of 1.5 mm diameter; within the test section sail models are sandwiched by a pair of circular observation panes by allowing the rods to penetrate panes through holes bored there; thus the sail models are set to rotate freely at the edges. By rotating the circular panes little by little, we change the angle of attack. Figure 3(b) shows the test section with a circular observation window.

First we set the model at $\alpha=20°$, and then we switch on the fan; by decreasing α by 1° at a time, we observe the model and take pictures at every angle of attack; we repeat this procedure until $\alpha=-20°$; then we stop the fan.

Next we set the model at $\alpha=-20°$, and then we switch on the fan; by increasing α by one degree at a time, we observe the model and take pictures at every angle of attack; we repeat this procedure until $\alpha=20°$; then we stop the fan.

IV. RESULTS AND DISCUSSION

A. Case studies of sail-sail-flow interactions: Numerical analysis

The problem has so many parameters, i.e., a, b, β, SR_j, and SR_m, that analyses, discussion, and annotation tend to be diverse. The present work confines our interest in the way that overlap affects aerodynamic and structural characteristics. We prepare one configuration for the largely overlapping case and two for the less overlapping cases. In the less overlapping cases, the x coordinate value of the trailing edge of the jib sail is smaller than the x coordinate value of the leading edge of the main sail. The fixed parameters are the slackness parameters, which are set to be 0.01 for both the sails. With this magnitude of the slackness parameter, the inviscid theory is known to agree fairly well with experiments in case of a single sail (see, for example, Refs. 4–6). In reality, slackness depends on the sailor's way of making sail, and it takes the value from the order of 0.01 to 0.1.[18]

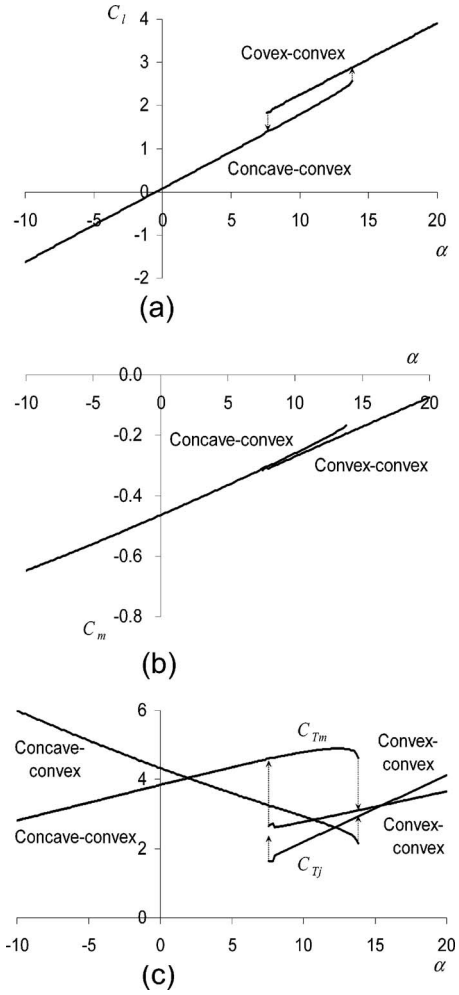

FIG. 4. Aerodynamic and structural characteristics of two sails with $SR_j=SR_m=0.01$, $a=1.0$, $b=-0.5$, and $\beta=10°$ from the theory. (a) C_l vs α; (b) C_m vs α; (c) C_{T_j}, C_{T_m} vs α; the transition from the convex-convex set to the concave-convex set occurs at $\alpha=7.6°$, while the transition from the concave-convex set to the convex-convex set occurs at $\alpha=13.8°$.

Before we go into detail of our new results, we summarize the bifurcation and hysteresis in single-sail phenomena.[7] The aerodynamic characteristics are odd functions of the angle of attack, while the tension is an even function of the angle of attack; at small angles of attack there are several equilibria, among which at least two are possible. This multiple existence of equilibria leads to hysteresis depending on the time history. At the zero angle of attack the formalism becomes the eigenvalue problem, which can be interpreted as "buckling in the air."

In the case of sail-sail-flow interactions there is no symmetry or asymmetry with respect to the angle of attack; the formalism does not pose the eigenvalue problem. But we interpret the phenomena as "buckling in the air." Now we shall see what happens to a pair of sails in a flow.

1. Case of largely overlapping sails from the theory

In this case the parameters are set in the following: $a=1.0$; $b=-0.5$; $\beta=10°$. Figures 4–6 show the results.

As shown in Fig. 4(a), the aerodynamic characteristics exhibit hysteresis because of the existence of bistability at

Downloaded 09 Dec 2007 to 61.204.235.6. Redistribution subject to AIP license or copyright; see http://pof.aip.org/pof/copyright.jsp

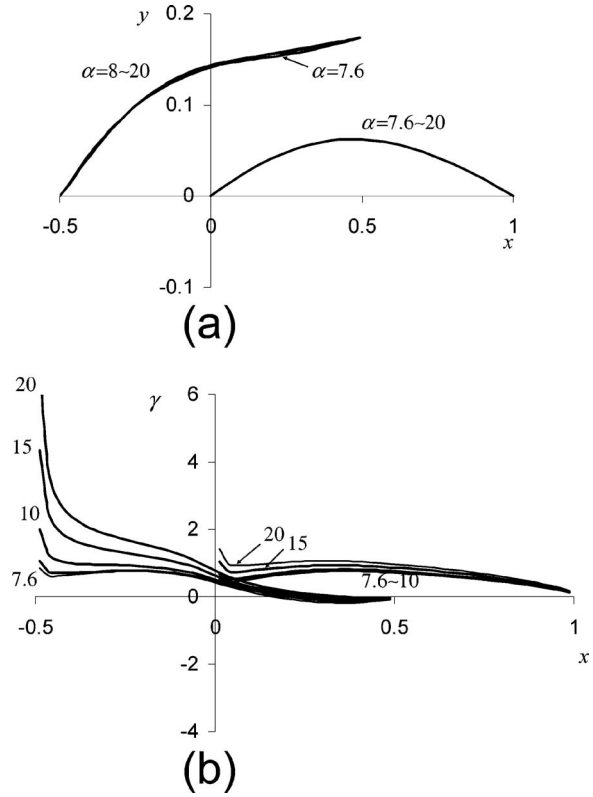

FIG. 5. Shapes in equilibrium and corresponding vorticity distributions of two sails with $SR_j = SR_m = 0.01$, $a = 1.0$, $b = -0.5$, and $\beta = 10°$: The convex-convex set from the theory (a) convex-convex shapes of two sails at various angles of attack larger than or equal to 7.7°; (b) corresponding vorticity distributions.

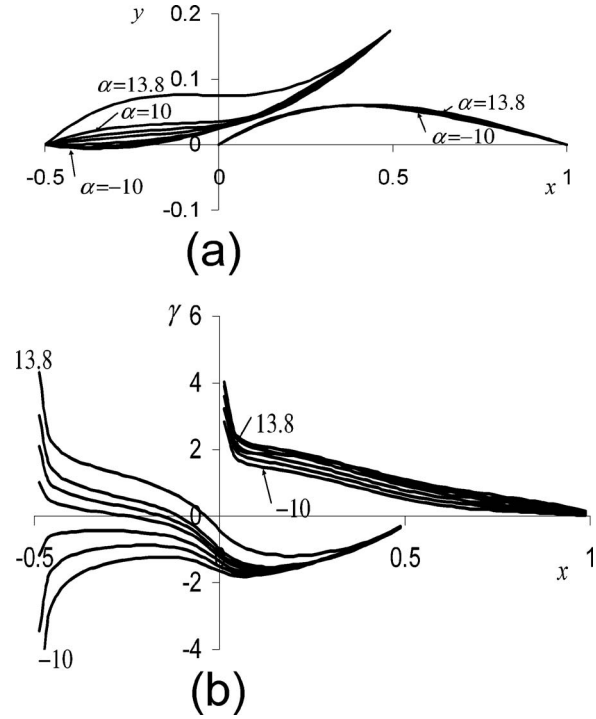

FIG. 6. Shapes in equilibrium and corresponding vorticity distributions of two sails with $SR_j = SR_m = 0.01$, $a = 1.0$, $b = -0.5$, and $\beta = 10°$: The concave-convex set from the theory (a) concave-convex shapes of two sails at various angles of attack less than or equal to 13.8°; (b) corresponding vorticity distributions.

$\alpha \in [7.6, 13.8]$ by the degree. The convex-convex set denotes the solution set starting from the solution uniquely convergent at $\alpha = 20°$ and consisting of the solutions obtained by changing α smaller little by little: A pair of convex sails appears. The concave-convex set denotes the solution set starting from the solution uniquely convergent at $\alpha = -20°$ and consisting of the solutions obtained by changing α larger little by little: A concave jib sail and a convex main sail appear. The convex-convex set does not exist at $\alpha < 7.6°$, while the concave-convex set exists at $\alpha \leqslant 13.8°$ only. We shall see the details in Figs. 5 and 6.

As shown in Fig. 4(b), hysteresis is also found in the moment. The nose-up moment about the mast, i.e., the leading edge of the main sail, is always negative. Although the jib sail yields the positive moment, the main sail contributes to generating the larger negative moment. The effective angle of attack for the jib sail is $\alpha - \beta$. Hence the moment becomes more negative as the angle of attack decreases. The moment decreases more and more as the angle of attack decreases in the concave-convex set. This is because even the jib sail yields the negative moment.

As shown in Fig. 4(c), the tensions exhibit hysteresis of a butterfly-type. The tension of the jib sail decreases more rapidly than that of the main sail. This is because the jib becomes loose as $\alpha - \beta$ approaches zero. The tension of the jib sail increases against decreasing α, while the tension of the main sail decreases against decreasing α. The major reason for these tendencies of tensions is attributed to the configuration of two sails. If the angle of attack is smaller than 10°, incoming flow approaches toward the jib sail first. Then the jib sail induces the flow field where air flows along the jib sail and the main sail is always in there. Thus against decreasing α the jib becomes tight and the main sail becomes loose at the same time.

As shown in Figs. 5(a) and 5(b), in the convex-convex set, both sails have camber lines curved upward and develop a positive lift. That means the jib sail works as a flap as expected. But the enhancement of lift is not twice as large as lift of the single sail. One of the reasons is that the main sail cannot generate much lift, as it is placed on the pressure side of the jib sail. This can be known by the vorticity distribution. Another reason lies in the rear part of the jib sail, which is slightly curved downward. This is due to the suction force in the vicinity of the main sail. The slightly inflected camber line of the jib sail develops negative vorticity in the vicinity of its trailing edge.

Figures 6(a) and 6(b) show shapes and vorticity distributions of the concave-convex set. In this set the jib and main sails get close together. If we blow air between two sheets of paper held parallel, then these sheets are sucked by low pressure in between. The same phenomenon occurs in the concave-convex set. This set exists at $\alpha \leqslant 13.8°$ and even at $\alpha = -30°$. Lift of the concave-convex set is always smaller than that of the convex-convex set insofar as both solutions coexist at $\alpha \in [7.7, 13.8]$ by the degree. The jib sail has camber lines curved downward and hence lift is almost always negative. Moreover even the suction force at the leading

Downloaded 09 Dec 2007 to 61.204.235.6. Redistribution subject to AIP license or copyright; see http://pof.aip.org/pof/copyright.jsp

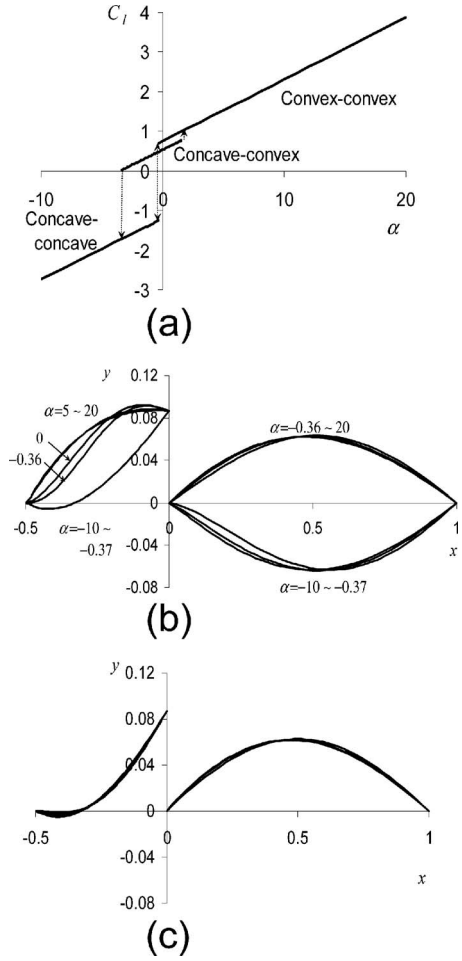

FIG. 7. Aerodynamic characteristics and shapes in equilibrium for the two sails with $SR_j=SR_m=0.01$, $a=0.5$, $b=-0.5$, and $\beta=10°$ from the theory. (a) C_l vs α; (b) convex-convex and concave-concave shapes of two sails at various angles of attack, among which the transition occurs at α in between $-0.37°$ and $-0.36°$; and (c) concave-convex shapes of two sails at various angles of attack in $[-3.4, 1.5]$ by the degrees.

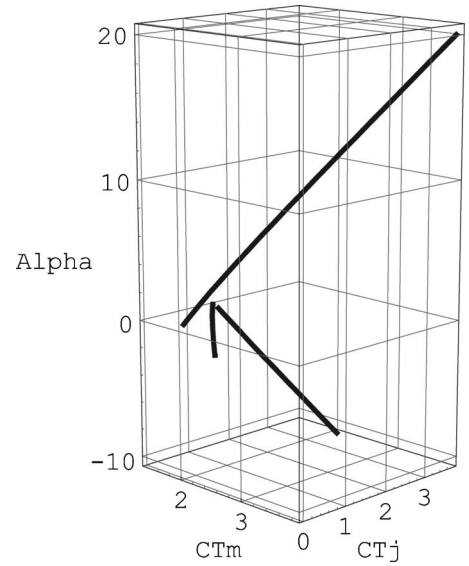

FIG. 8. Bifurcation diagram: The solution sets in the three parameter space for the two sails with $SR_j=SR_m=0.01$, $a=0.5$, $b=-0.5$, and $\beta=10°$ from the theory. The solid lines show the three solution sets in $(C_{T_m}, C_{T_j}, \alpha)$ space.

edge becomes negative at the negative angle of attack. This means the stagnation point is located at the upper surface of the sail.

In summary, we find two solution sets and hence hysteresis in aerodynamic and structural characteristics. With respect to the evaluation of overlapping, it is less advantageous that we overlap two sails too much as the configurations mentioned here. In such a case the enhancement of lift due to addition of the jib sail is not so large, and two sails are prone to get close together. Therefore it is not recommended to use the same-size jib and main sails close together; if we do so, the use is confined at the angle of attack larger than 15°.

2. Case of less overlapping sails: A small jib sail from the theory

This is the case that a smaller jib sail with $a=0.5$ is set at $b=-0.5$ and $\beta=10°$. Figures 7 and 8 show the results. Since we concentrate our consideration for understanding bifurcation and hysteresis, we put aside less illustrative vorticity distributions, C_m-α and C_{T_i}-α curves in the consecutive subsections on numerical analysis on the cases of less overlapping sails.

Figure 7(a) shows the C_l-α curve, which exhibits twofold hysteresis. In this case we find another solution set, i.e., the concave-concave set. Interestingly numerical calculation transits from the convex-convex set at $\alpha=-0.36°$ to the concave-concave set at $\alpha=-0.37°$ very smoothly. It is appropriate to consider these solution sets before and after $\alpha=-0.36°$ constitute the physically meaningful one set of solutions. Since we find this transition, we hunt for another solution around this discontinuity to find the concave-convex set as a result. This set exists at $\alpha \in [-3.4, 1.5]$ by the degree. Quantity of lift is in the following order: the concave-concave set; the concave-convex set; the convex-convex set. The lift of the convex-convex set is large enough compared to the largely overlapping sails mentioned in the previous subsection, although added sail area is half of that for the largely overlapping sails. Therefore it is recommended to use the half-size jib and full-size main sails for enhancing the lift in almost all the range of the positive angle of attack. Such a jib sail acts as "a leading-edge flap."

Figure 7(b) shows the sail shapes for the convex-convex and concave-concave sets. At the high angle of attack both sails have camber lines curved upward; around $\alpha=0°$ the jib sail exhibits inflected camber line but the main sail holds almost the same shape as that at the high angle of attack; at $\alpha=-0.36°$ the jib sail has an S-camber but with still positive lift, while the main sail stays almost the same; at $\alpha=-0.37°$ the jib and main sails become curved downward at the same time and both the sails stay almost the same against α decreasing.

Figure 7(c) shows the sail shapes for the concave-convex set. This set of solutions exists only at $\alpha \in [-3.4, 1.5]$ by the degree. If decreasing α causes reversal of camber of the jib

Downloaded 09 Dec 2007 to 61.204.235.6. Redistribution subject to AIP license or copyright; see http://pof.aip.org/pof/copyright.jsp

sail slightly earlier in timing than that of the main sail at the discontinuous point, i.e., $\alpha=-0.36°$, the convex-convex set transits to the concave-convex set. Once the channel between two sails is formed, low pressure sucks two sails. In this configuration the jib sail is tight, while in the wake of the jib sail the main sail is loose. At $\alpha=-3.4°$ reversal of camber of the main sail occurs, and the concave-convex set transits to the concave-concave set. Similarly at $\alpha=1.5°$ reversal of camber of the jib sail occurs, and the concave-convex set transits to the convex-convex set. Thus hysteresis becomes twofold.

Figure 8 is the bifurcation diagram for the present problem showing the solution sets as thick solid curves in $(C_{T_m}, C_{T_j}, \alpha)$ space, where α is measured by the degree. We see three curves do not intersect one another in this parameter space. The convex-convex set lies between $(1.65, 0.48, -0.36°)$ and (3.85, 3.74, 20°); the concave-convex set lies between $(1.56, 1.35, -3.44°)$ and (2.09, 0.57, 1.53°); the concave-concave set lies between $(2.33, 3.28, -10°)$ and $(1.38, 1.68, -0.37°)$. In the concave-convex set $(C_{T_m}, C_{T_j}) = (1.88, 0.85)$ around $\alpha=-0.36°$. In any cases sails become loose near $\alpha=-0.36°$, and hence the transition takes place around this angle of attack. The Newton–Raphson method drives the search toward the solution in the constant α plane in this $(C_{T_m}, C_{T_j}, \alpha)$ space. In this particular case we may encounter two solutions in the constant α plane.

3. Case of less overlapping sails: A large jib sail from the theory

This is the case that a jib sail with $a=1.0$ is set more upstream at $b=-1.0$ and $\beta=5.0°$. Figure 9 shows the results of the numerical analysis.

Figure 9(a) shows the C_l-α curve. The phenomena are quite similar to those annotated in the previous subsection. While the convex-convex set and the concave-concave set exist complimentarily at all α calculated in between ±20°, the concave-convex set coexists with the other set at $\alpha \in [-14.1, 1.5]$ by the degree. The transition between the convex-convex set and the concave-concave set takes place at $\alpha=-1.9°$. Spanning the jib sail generates one and a half times larger lift than the main sail alone, if $\alpha \geqslant -1.9°$. This type of large jib sail, however, changes the characteristics of the nose-up moment, $\partial C_m/\partial\alpha$ is negative for the single sail, $\partial C_m/\partial\alpha$ is positive for a pair of sails, and the large jib is located ahead of the mast. Therefore we have to change the way of controlling the direction of a sailing craft, if we span such a large jib sail.

As shown in Fig. 9(b) at $\alpha \geqslant -1.9°$ both the sails have camber lines curved upward, while at $\alpha \leqslant -1.9°$ both the sails have camber lines curved downward. The jib sail assumes the S-camber at $\alpha=-1.9°$, which implies the tension is small. When the tensions become small, the transition between the convex-convex set and the concave-concave set occurs.

Figure 9(c) shows the shapes of the concave-convex set, in which two sails get close together. This set yields larger lift than the convex-convex set at $\alpha \leqslant -1.9°$, because the main sail holds the camber curved upward. Reversal of the camber of the main sail occurs at $\alpha=-14.1°$, if we decrease the angle of attack further; then the concave-concave set appears. Reversal of the camber of the jib sail occurs at $\alpha=1.5°$, if we increase the angle of attack further; then the convex-convex set appears.

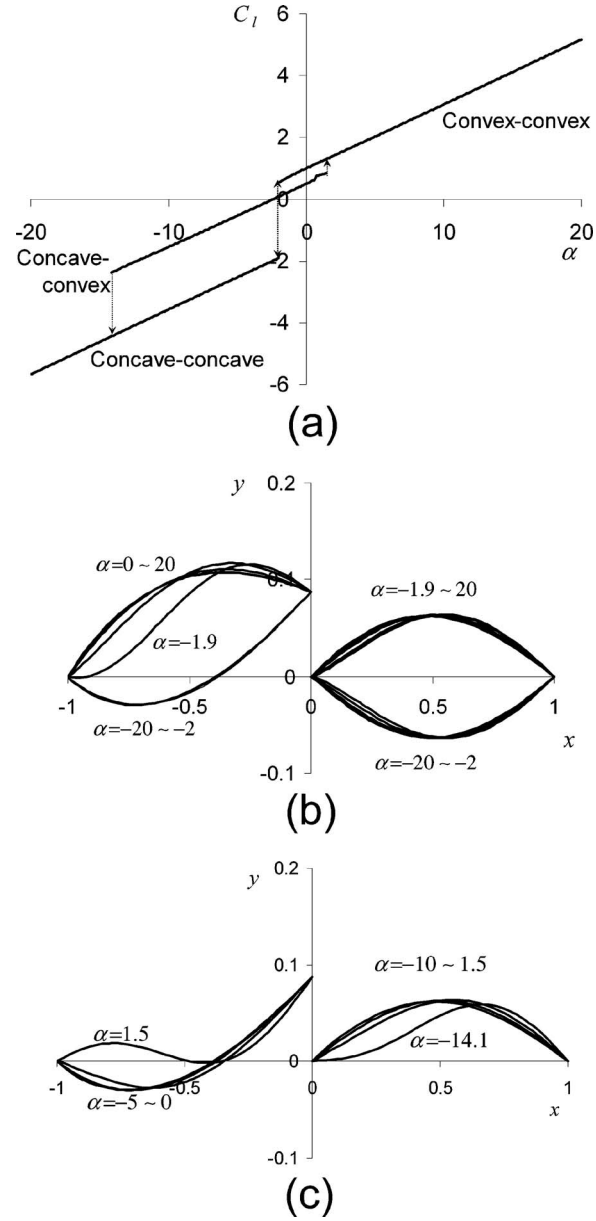

FIG. 9. Aerodynamic characteristics and shapes in equilibrium for the two sails with $SR_j=SR_m=0.01$, $a=1.0$, $b=-1.0$, and $\beta=5.0°$ from the theory. (a) C_l vs α; (b) convex-convex and concave-concave shapes of two sails at various angles of attack, among which the transition occurs at $\alpha=-1.9°$; and (c) concave-convex shapes of two sails at various angles of attack in $[-14.1, 1.5]$ by the degrees.

Comparing the result of largely overlapping sails, we conclude as follows: The same-size jib and main sails should be laid out as staggered and no overlapping, then the lift is greatly enhanced in almost all the range of the positive angle of attack. This is summarized as the "double main-sail effect."

Downloaded 09 Dec 2007 to 61.204.235.6. Redistribution subject to AIP license or copyright; see http://pof.aip.org/pof/copyright.jsp

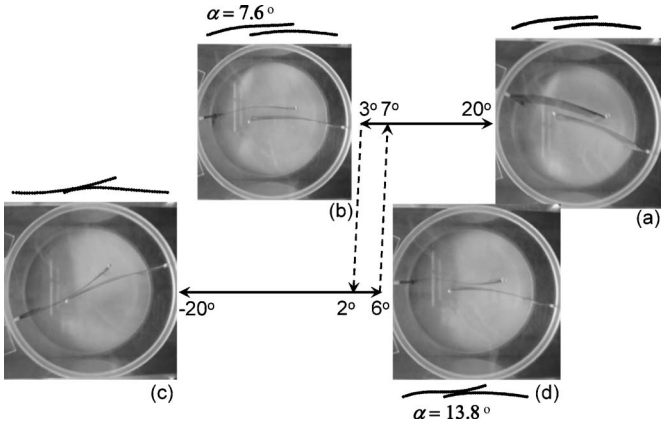

FIG. 10. Shapes in equilibrium observed in the experiments for the two sails with $SR_j = SR_m = 0.01$, $a = 1.0$, $b = -0.5$, and $\beta = 10°$. (a) The convex-convex shape at $\alpha = 20°$; (b) the convex-convex shape at $\alpha = 3.0°$; (c) the concave-convex shape at $\alpha = -20°$; (d) the concave-convex shape at $\alpha = 6.0°$; line drawings adjacent to photos show the counterparts from the theory; their angles of attack are the same as the experiments unless otherwise labeled differently; the transition from the convex-convex set to the concave-convex set is predicted by the theory to occur at $\alpha = 7.6°$, while the transition from the concave-convex set the convex-convex set at $\alpha = 13.8°$.

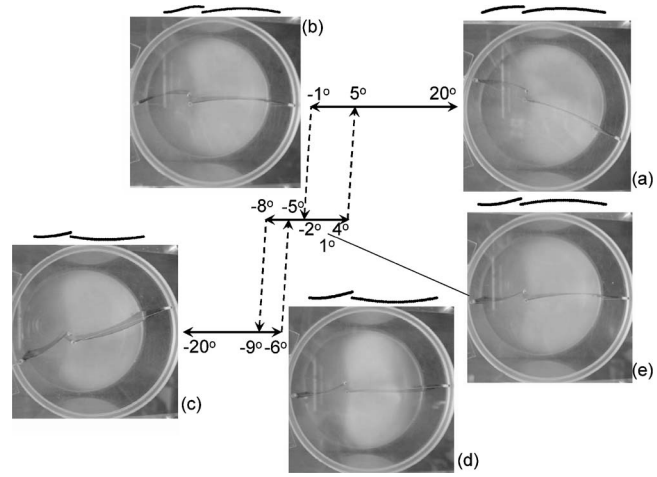

FIG. 11. Shapes in equilibrium observed in the experiments for the two sails with $SR_j = SR_m = 0.01$, $a = 0.5$, $b = -0.5$, and $\beta = 10°$. (a) The convex-convex shape at $\alpha = 20°$; (b) the convex-convex shape at $\alpha = -1.0°$; (c) the concave-concave shape at $\alpha = -20°$; (d) the concave-concave shape at $\alpha = -6.0°$; (e) the concave-convex shape at $\alpha = 1.0°$; line drawings adjacent to photos show the counterparts from the theory at the same angles of attack as the experiments; the convex-convex set and the concave-concave set are predicted by the theory to exist complementary to α in between $-0.37°$ and $-0.36°$, while the concave-convex set is predicted by the theory to exist at α in $[-3.4, 1.5]$ by the degrees.

B. Case studies of sail-sail-flow interactions: Experimental observations

Motivated by the prediction about complex bifurcation and hysteresis phenomena in sail-sail-flow interactions due to our numerical analysis, we prepare experiments to see if the prediction is true or spurious. Experimental conditions are as follows: The air speeds range from 20 to 22 m/s; the resulting Reynolds number defined by the chord length of the main sail is $7.8-8.3 \times 10^4$.

In the following figures all the pictures are rearranged to fit to the coordinate system defined by Fig. 1: The uniform flow comes from the left of the pictures; if the leading edge of the main sail is lifted upward, its angle of attack is positive, and vice versa. Line drawings adjacent to photos show the counterparts from the theory. Their angles of attack are the same as the experiments unless otherwise labeled differently.

1. Case of largely overlapping sails from the experiments

Figure 10 shows the schematic summary of the experimental counterparts for the case of largely overlapping sails; the parameters are set in the following: $a = 1.0$, $b = -0.5$, $\beta = 10°$.

At $\alpha = 20°$ we observe the convex-convex set as shown in Fig. 10(a), which stably exists until $\alpha = 3.0°$ as shown in Fig. 10(b). At $\alpha = 2.0°$, reversal of camber in the jib sail occurs, and the concave-convex set appears until $\alpha = -20°$. We observe occasional benign flatter in the concave-convex set at $\alpha \in [-11, -2.0]$ by the degree, while the concave-convex sails cease to flatter at $\alpha \in [-20, -12]$ by the degree. Therefore the concave-convex set is not intrinsically unstable.

We restart the experiments at $\alpha = -20°$ as shown in Fig. 10(c), and there is the concave-convex set. This set exists up to $\alpha = 6.0°$; at $\alpha \geqslant -14°$ we occasionally observe benign flatter. As shown in Fig. 10(d), the jib sail assumes S-camber at $\alpha = 6.0°$. At $\alpha = 7.0°$ reversal of camber in the jib occurs, and the convex-convex set appears until $\alpha = 20°$.

In the experiments the transition from the convex-convex set to the concave-convex set occurs at α in between 2.0° and 3.0°, while this transition is predicted by the theory to occur at $\alpha = 7.6°$. In the experiments the transition from the concave-convex set to the convex-convex set occurs at α in between 6.0° and 7.0°, while this transition is predicted by the theory to occur at $\alpha = 13.8°$.

The theory succeeds in predicting what kind of phenomena occurs. Theoretical shapes in equilibrium are in good agreement with those observed in the experiments, but there are some discrepancies in the angles of attack.

2. Case of less overlapping sails: A small jib sail from the experiments

Figure 11 shows the schematic summary of the experimental counterparts for the case of less overlapping sails with a small jib sail; the parameters are set in the following: $a = 0.5$ is set at $b = -0.5$ and $\beta = 10°$.

At $\alpha = 20°$ we observe the convex-convex set as shown in Fig. 11(a), which stably exists until $\alpha = -1.0°$ as shown in Fig. 11(b). At $\alpha = -2.0°$, reversal of camber in the jib sail occurs, and the concave-convex set appears until $\alpha = -8.0°$. No noticeable flatter occurs in this concave-convex set. At $\alpha = -9.0°$, reversal of camber in the main sail occurs, and the concave-concave set appears until $\alpha = -20°$.

We restart the experiments at $\alpha = -20°$ as shown in Fig. 11(c), and there is the concave-concave set. This set exists until $\alpha = -6.0°$ as shown in Fig. 11(d). At $\alpha = -5.0°$, reversal of camber in the main sail occurs, and the concave-convex

Downloaded 09 Dec 2007 to 61.204.235.6. Redistribution subject to AIP license or copyright; see http://pof.aip.org/pof/copyright.jsp

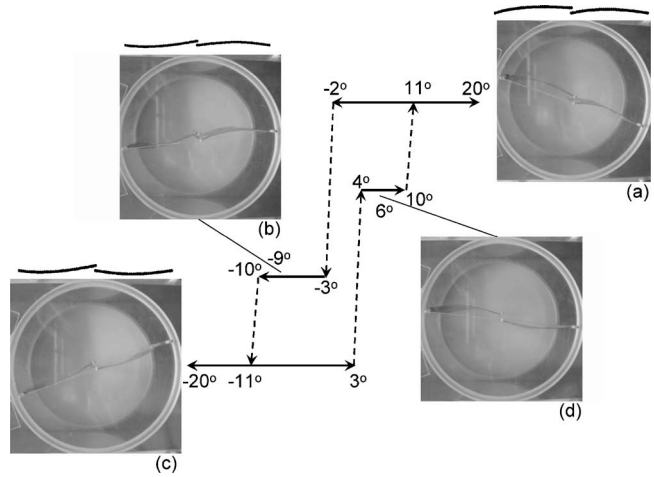

FIG. 12. Shapes in equilibrium observed in the experiments for the two sails with $SR_j=SR_m=0.01$, $a=1.0$, $b=-1.0$, and $\beta=5.0°$. (a) The convex-convex shape at $\alpha=20°$; (b) the concave-convex shape at $\alpha=-9.0°$; (c) the concave-concave shape at $\alpha=-20°$; (d) the convex-concave shape at $\alpha=6.0°$; line drawings adjacent to photos show the counterparts from the theory at the same angles of attack as the experiments; the convex-convex set and the concave-concave set are predicted by the theory to exist complementary to $\alpha=-1.9°$, while the concave-convex set is predicted by the theory to exist at α in $[-14.1, 1.5]$ by the degrees.

set appears until $\alpha=4.0°$ as shown in Fig. 11(e). At $\alpha=5.0°$, reversal of camber in the jib sail occurs, and the convex-convex set appears until $\alpha=20°$.

In the experiments the transition from the convex-convex set to the concave-convex set occurs at α in between $-2.0°$ and $-1.0°$, while this transition is predicted by the theory to occur at α in between $-0.37°$ and $-0.36°$. In the experiments the transition from the concave-concave set to the concave-convex set occurs at α in between $-6.0°$ and $-5.0°$, while this transition is predicted by the theory to occur at α in between $-0.37°$ and $-0.36°$. In the experiments we observe the concave-convex set at α in $[-8.0, 4.0]$, by the degrees, while the theory predicts the existence of the concave-convex set at α in $[-3.4, 1.5]$ by the degrees. The experimental results suggest the concave-convex set may be more stable than other equilibria at small angles of attack. This is because the strong channel flow exists between sails and this low-pressure flow sucks both the sails.

Thus the theory succeeds to predict what kind of phenomena occurs. Theoretical shapes in equilibrium are in good agreement with those observed in the experiments, but there are some discrepancies in transition angles.

3. Case of less overlapping sails: A large jib sail from the experiments

Figure 12 shows the schematic summary of the experimental counterparts for the case of less overlapping sails with a large jib sail; the parameters are set in the following: $a=1.0$ is set more upstream at $b=-1.0$ and $\beta=5.0°$.

At $\alpha=20°$ we observe the convex-convex set as shown in Fig. 12(a), which stably exists until $\alpha=-2.0°$. At $\alpha=-3.0°$ reversal of camber in the jib sail occurs, and the concave-convex set appears until $\alpha=-10°$. No noticeable flatter occurs in this concave-convex set. The sample shape at $\alpha=-9.0°$ is shown in Fig. 12(b). At $\alpha=-11.0°$ reversal of camber in the main sail occurs, and the concave-concave set appears until $\alpha=-20°$.

We restart the experiments at $\alpha=-20°$ as shown in Fig. 12(c), and there is the concave-concave set. This set exists until $\alpha=3.0°$. At $\alpha=4.0°$, reversal of camber in the jib occurs, and the convex-concave set appears until $\alpha=10°$. As shown in Fig. 12(e) this convex-concave set is found by experiments only. At $\alpha=11°$ reversal of camber in the main sail occurs, and the convex-convex set appears until $\alpha=20°$.

In the experiments the transition from the convex-convex set to the concave-convex set occurs at α in between $-3.0°$ and $-2.0°$, while this transition is predicted by the theory to occur at $\alpha=-1.9°$. In the experiments the transition from the concave-convex set to the concave-concave set occurs at α in between $-11.0°$ and $-10.0°$, while this transition is predicted by the theory to occur at $\alpha=-14.5°$. In the experiments we observe the unexpected transition from the concave-concave set to the convex-concave set at α in between $3.0°$ and $4.0°$. With this almost-no-overlap layout of sails there are a few chances for the formation of channel flow between the sails.

Thus the theory succeeds to predict what kind of phenomena occurs. Theoretical shapes in equilibrium are in good agreement with those observed in the experiments, but there are minor discrepancies in transition angles.

After the experiments we search for the convex-concave set by the simulations, but so far we could not find this particular set by our numerical analysis. The most plausible reason for the alibi lies on the point that we neglect the effect of gravity, because gravity pulls the sail to the right in these pictures.

V. CONCLUSIONS

We summarize our findings as follows:

(1) As a representation of sail-sail-flow interactions, we introduce the tractable formalism consisting of a pair of integro-differential equations, equivalent to Fredholm equations of the second kind, subject to a pair of nonlinear integral constraints.
(2) To solve the basic equations subject to the constraints and boundary conditions, we invent the method of solution consisting of the vortex lattice method and the Newton–Raphson method, which captures multiple solutions for sail-sail-flow interactions; these are the convex-convex set, the concave-convex set, and the concave-concave set.
(3) We discover the complex bifurcation and manyfold hysteresis phenomena in sail-sail-flow interactions predicted by the numerical analysis and verified qualitatively by the experimental observations; another equilibrium, the convex-concave set, is found by the experiments only.
(4) We evaluate how overlap of a jib sail upon a main sail affects, and find too much overlap of sails fails to obtain

Downloaded 09 Dec 2007 to 61.204.235.6. Redistribution subject to AIP license or copyright; see http://pof.aip.org/pof/copyright.jsp

high lift. This is because the concave-convex set comes to existence due to the possible channel-flow formation between overlapping sails.

Everything has just started, so there are a lot of things to do. The following are the main menu of the future challenges: we should study stability of equilibria; we should consider neglected effects, e.g., mass of sails, viscosity, and so forth; we should extend the formalism and the method of solution to three-dimensional problems; we should look for the optimum configuration of two sails in the line of the present formalism; thorough quantitative experiments are of course necessary.

[1]K. Voelz, "Profil und auftrieb eines segels," Z. Angew. Math. Mech. **30**, 22 (1950).
[2]B. Thwaites, "The aerodynamic theory of sails," Proc. R. Soc. London, Ser. A **201**, 402 (1961).
[3]J. N. Nielsen, "Theory of flexible aerodynamic surfaces," ASME J. Appl. Mech. **30**, 435 (1963).
[4]B. G. Newman and H. T. Low, "Two-dimensional impervious sails: Experimental results compared with theory," J. Fluid Mech. **144**, 445 (1984).
[5]S. Greenhalgh, H. C. Curtiss, Jr., and B. Smith, "Aerodynamic characteristics of two-dimensional inextensible flexible airfoil," AIAA J. **22**, 865 (1984).
[6]T. Sugimoto and J. Sato, "Aerodynamic characteristics of two-dimensional membrane airfoils," Trans. Jpn. Soc. Aeronaut. Space Sci. **34**, 88 (1991).
[7]H. Murai and S. Maruyama, "Possibility of various airfoil shape modes and their steady state stability of single membrane sail wings," Bull. JSME **27**, 450 (1986).
[8]P. S. Jackson and S. P. Fiddes, "Two-dimensional viscous flow past flexible sail sections close to ideal incidence," Aeronaut. J. **99**, 217 (1995).
[9]R. Smith and W. Shyy, "Computation of aerodynamic coefficients for a flexible membrane airfoil in turbulent flow: A comparison with classical theory," Phys. Fluids **8**, 3346 (1996).
[10]P. S. Jackson and G. W. Christie, "Numerical analysis of three-dimensional elastic membrane wings," AIAA J. **25**, 676 (1987).
[11]T. Sugimoto, "Analysis of circular elastic membrane wings," Trans. Jpn. Soc. Aeronaut. Space Sci. **34**, 153 (1991).
[12]K. L. E. Nickel, "A theory of sail-wings," Z. Flugwiss. Weltraumforsch. **11**, 321 (1987).
[13]M. Wohlfahrt, "Die auftriebsverteilung von flexiblen segel längs der spann weite," Z. Angew. Math. Mech. **67**, 281 (1987).
[14]T. Sugimoto, "Wing design for hang gliders having minimum induced drag," J. Aircr. **29**, 730 (1992).
[15]T. Sugimoto, "A theory for inextensible and high aspect-ratio sails," J. Wind. Eng. Ind. Aerodyn. **63**, 61 (1996).
[16]P. S. Jackson, "Theory for conical membrane wings of high aspect ratio," AIAA J. **39**, 781 (2001).
[17]J. O. Myall and S. A. Berger, "Interaction between a pair of two-dimensional sails for the case of smoothly attached flow," Proc. R. Soc. London, Ser. A **310**, 373 (1969).
[18]P. S. Jackson, "Two-dimensional sails in inviscid flow," J. Ship Res. **28**, 11 (1984).
[19]A. M. Kuethe and C.-Y. Chow, *Foundations of Aerodynamics: Basis of Aerodynamic Design*, 4th ed. (Wiley, Singapore, 1988).
[20]J. Katz and A. Plotkin, *Low-Speed Aerodynamics*, 2nd ed. (Cambridge University Press, Cambridge, 2001).
[21]F. G. Tricomi, *Integral Equations*, Dover edition (Dover, New York, 1985).

Downloaded 09 Dec 2007 to 61.204.235.6. Redistribution subject to AIP license or copyright; see http://pof.aip.org/pof/copyright.jsp